Thiometallate-mediated polysulfide chemistry and lithium stabilization for stable anode-free lithium-sulfur batteries

Sanjay Nanda, Hooman Yaghoobnejad Asl, Amruth Bhargav, and Arumugam Manthiram[*]

Materials Science and Engineering Program and Texas Materials Institute, The University of Texas at Austin, Austin, Texas 78712, United States of America

Summary

Achieving long cycle life with energy-dense lithium-sulfur (Li-S) batteries require improving the reversibility of lithium plating and stripping. This problem is rendered unique in the Li-S system by the formation of soluble polysulfide intermediates, which degrade the lithium-metal anode by reducing into insulating Li_2S and Li_2S_2. We have discovered that the introduction of ammonium tetrathiomolybdate $((NH_4)_2MoS_4)$ and ammonium tetrathiotungstate $((NH_4)_2WS_4)$ as cathode additives stabilize lithium deposition by (i) complexing with polysulfides and acting as a polysulfide buffer, thereby mitigating the corrosive shuttle effect, and (ii) forming a stable and passivating molybdenum and tungsten-enriched solid-electrolyte interphase (SEI) layer on the lithium surface. The resulting stabilization of lithium electrodeposition enables a nearly three-fold improvement in the cycle of anode-free full cells assembled with no excess lithium inventory. This work demonstrates that the rich chemistry of thiometallate complexes and polysulfide species in solution can be exploited to solve the formidable challenges with achieving a realistic lithium-sulfur battery, and more generally metal-chalcogen batteries.

---

[*]Corresponding author: Tel: +1-512-471-1791; fax: +1-512-471-7681.
E-mail address: manth@austin.utexas.edu (A. Manthiram)

Introduction

The intrinsic energy density and cost advantages of lithium-sulfur (Li-S) batteries are undermined by the excess lithium and electrolyte that is required in the cell to compensate for the amount lost during cycling, which otherwise causes severe capacity fade.[1–4] This problem is uniquely exacerbated in the Li-S system by the generation of polysulfide species (S_x^{2-}) that diffuse to the lithium-metal anode, causing unwanted parasitic side reactions that exhaust the limited lithium reservoir. In order for Li-S batteries to realize their full potential, two practical hurdles need to be addressed at a fundamental level: (1) the polysulfide shuttle and side reactions with the lithium-metal anode has to be suppressed, and (2) a stable and protective solid-electrolyte interphase (SEI) layer should be designed, such that the initial amount of lithium and electrolyte loaded into the cell can be minimized.[5,6]

Previously, there have been multiple attempts to address the first issue through an immobilization of the soluble S_x^{2-} species on solid substrates via various intermolecular interactions ranging from weak van der Waals forces to stronger Lewis acid-base coordination.[2,7–9] However, achieving effective interaction between the substrate and S_x^{2-} species in the liquid phase necessitates maximizing the surface area of the substrate through extensive down-sizing, which aggravates the need for excess electrolyte loading due to an uptake by the porous substrate. The second issue is challenging due to the dynamic nature of mossy lithium growth and concomitant large volume changes, which precludes the implementation of a static artificial SEI layer with high Li^+ mobility.

In this work, we demonstrate a novel homogenous-phase approach that presents a unified solution to the two fundamental challenges outlined above. This approach exploits the solution chemistry of thiometallate anions, MS_4^{2-} (M: Mo, W), which play a dual role

in suppressing the factors that cause a premature failure of Li-S batteries. On one hand, the MS_4^{2-} anions can undergo a series of transformations to incorporate neutral sulfur atoms (S^0) present in polysulfide (S_x^{2-}) chains, thereby suppressing their antagonistic reactions with the high-surface area mossy lithium deposit. On the other hand, the recursive supply of dissolved MS_4^{2-} anions into the electrolyte from a solid source that is blended with the cathode enables the formation of a passivating, self-healing SEI layer on the lithium surface enriched with Mo and W-species.

The consequent stabilization of lithium deposition allows pursuing the radical strategy of fabricating "anode-free" Li-S cells assembled in the discharged state with a lithium sulfide (Li_2S) cathode, which serves as the source of both active lithium and sulfur, and a bare current collector on the anode side. With the introduction of MoS_4^{2-} and WS_4^{2-} anions into the system, the cycle life of anode-free full cells can be extended by a factor of ~ 3, from 58 cycles to 164 cycles. The approach presented here is expected to open a new avenue for helping solve the formidable challenges with Li-S batteries and bring them one step closer to realizing their full potential.

Results and Discussion

Introducing thiometallate anions into the electrolyte

Thiometallates are known to act as sulfur donors and acceptors and thus form the core of biologically important metalloenzymes.[10,11] Due to their ability to easily interact with sulfur, thiometallate clusters of molybdenum and tungsten have been exploited as catalysts in the hydrodesulfurization of crude oil.[12,13] Recently, thiomolybdate clusters have been shown as good hydrogen-evolution catalysts as well.[14] These complexes owe

their versatility to the covalent nature of the transition metal-sulfur bond. This intrigued us to study the interaction of dissolved thiomolybdate ($Mo_xS_y^{2-}$) and thiotungstate ($W_xS_y^{2-}$) species with polysulfides. Commercially available ammonium tetrathiomolybdate (($NH_4)_2MoS_4$, ATTM) and ammonium tetrathiotungstate (($NH_4)_2WS_4$, ATTW) are not soluble in the ether-based 1,3-dioxolane (DOL) or 1,2-dimethoxyethane (DME) solvents. However, we discovered that when Li_2S powder and ATTM or ATTW were stirred together in DOL/DME (1 : 1, vol.), colored solutions were obtained – dark red in the case of ATTM and bright yellow-green in the case of ATTW (**Figure 1a**). To identify the dissolved species, the colored solutions were drop-cast onto an inert silicon wafer, and the dried residue was analyzed with X-ray photoelectron spectroscopy (XPS). As shown with the Mo 3p and W 4f spectra in **Figure 1b** and **c**, clear evidence is obtained for the formation of dissolved thiomolybdate ($Mo_xS_y^{2-}$) and thiotungstate ($W_xS_y^{2-}$) species when Li_2S is mixed with ATTM and ATTW, respectively.[15,16] Furthermore, when compared with the peak positions for Mo^{6+} and W^{6+} in commercial ($NH_4)_2MoS_4$ and ($NH_4)_2WS_4$, it can be seen that the formation of dissolved $Mo_xS_y^{2-}$ and $W_xS_y^{2-}$ species is accompanied by a reduction of the Mo^{6+} and W^{6+} ions, which indicates charge-transfer between the metal center and the sulfur ligands.[17]

$$(NH_4^+)_2[M^{(6+)}S_4]_{(s)} + Li_2S_{(s)} \rightarrow Li_x[M^{(5+/6+)}S_4]^{2-}_{(sol)} + (NH_4)_yS^{2-}_{(sol/s)}$$
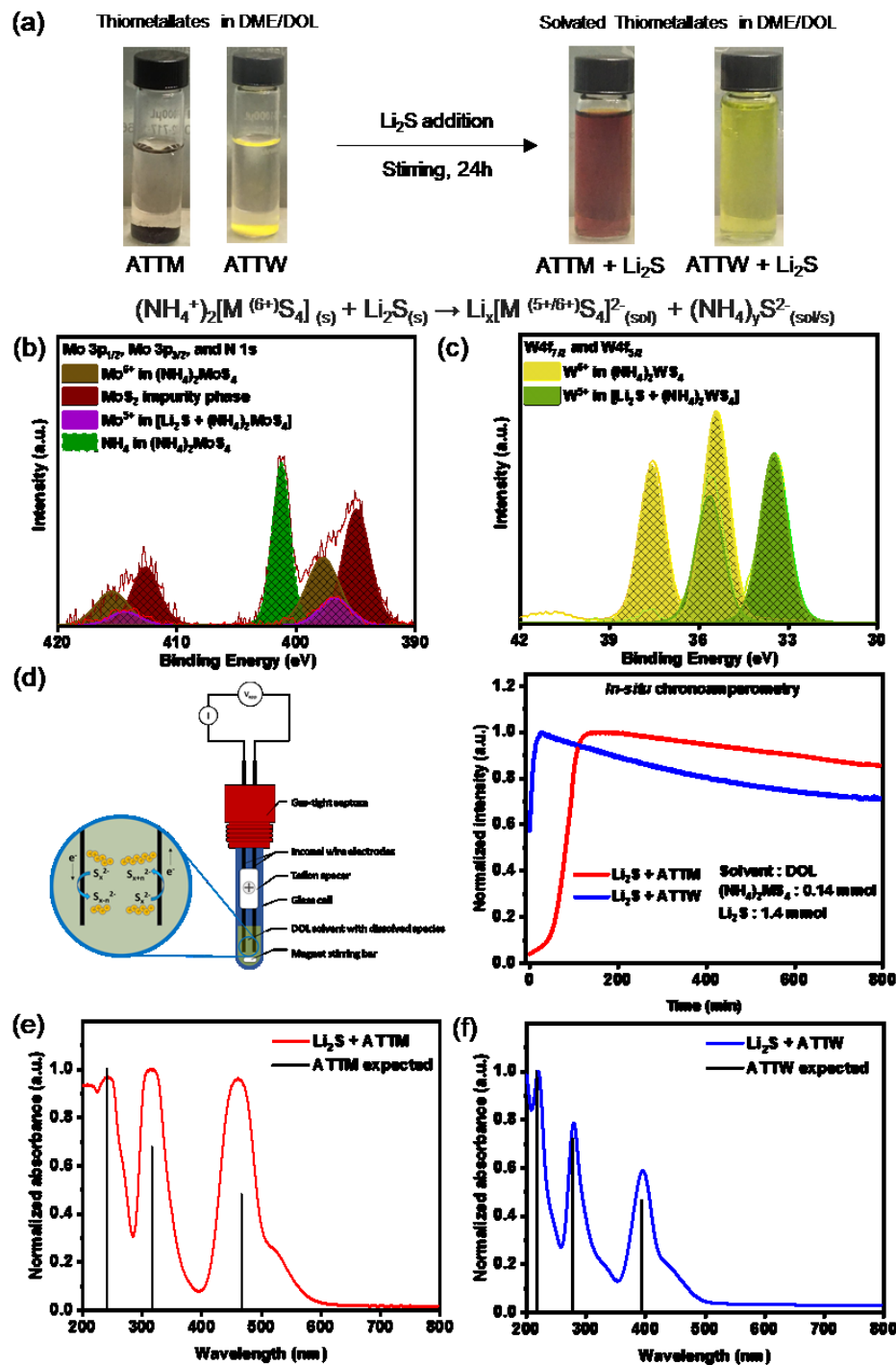
Fig. 1 | Characterization of MS$_4^{2-}$ thiometallate species in the ether-based electrolyte. a, Photographs visually showing the interaction between thiometallates and Li$_2$S. **b**, **c**, XPS spectra of, respectively, MoS$_4^{2-}$ and WS$_4^{2-}$ species in DME/DOL electrolyte upon reaction with Li$_2$S. **d**, Schematic of the *in-situ* chronoamperometric study setup and the curves of (NH$_4$)$_2$MS$_4$ – Li$_2$S reaction, indicating the rate of introduction of redox-active MS$_4^{2-}$ species in the electrolyte. **e**, **f**, UV-Vis absorption spectra of MS$_4^{2-}$ species upon reaction with Li$_2$S, and its comparison with the observed peak positions for aqueous solutions of MS$_4^{2-}$ species (M: Mo, W).

5

To further investigate this reaction, it was monitored *in-situ* via chronoamperometry for a mixture of Li_2S and ATTM or ATTW in DOL. Despite the negligible solubility of these reactants, the current rose sharply from the initial background, and the solution color changed from clear to dark red for ATTM and bright yellow-green for ATTW. This indicates the introduction of electroactive $Mo_xS_y^{2-}$ and $W_xS_y^{2-}$ species into the solvent. The measured current peaked at 150 minutes for ATTM, while the peak was reached after 30 minutes for ATTW (**Figure 1d**), indicating that the rate of thiotungstate dissolution is significantly faster than that of the thiomolybdate in the electrolyte.

UV-Vis spectra of the thiomolybdate and thiotungstate solutions in DOL/DME solvent indicate sharp absorption bands (**Figure 1e** and **f**), indicating well-defined molecular entities. A comparison with the UV-Vis spectra for Li_2S_8 rules out the presence of polysulfides and an underlying redox reaction pathway. Therefore, the reaction between Li_2S and ATTM/ATTW can be described as a Lewis acid-base reaction via a double-displacement mechanism, mediated through hydrogen-bonding between NH_4^+ and S^{2-}:

$$(NH_4)_2[M^{(6+)}S_4]_{(s)} + Li_2S_{(s)} \rightarrow Li_x[M^{(6+)}S_4]^{2-}_{(sol)} + (NH_4)_yS^{2-}_{(sol/s)}$$
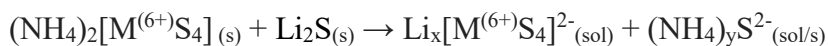
The above assertion was validated through a comparison of the observed UV-Vis peak positions for MoS_4^{2-} and WS_4^{2-} in aqueous solutions, which gives almost identical absorption behavior to the current case.[11,18] Also, it has been shown that the shift in absorption maxima and relative intensities from aqueous solutions of $(NH_4)_2MS_4$ species to acetonitrile solutions of $(NH_4)_2MS_4$ is less than, respectively, 5 nm and 10 % in all cases. This indicates the minor effect of the solvent on the electronic absorption spectra of MS_4^{2-} species, also proven by recording UV-Vis spectra of $(NH_4)_2MS_4$ in DMF (**Figure S1**). Finally, a calculation of optical transitions for a hypothetical Li_2MoS_4 molecule in DOL

based on density functional perturbation theory (DFPT) yields a theoretical absorption spectrum that matches the observed spectra within the margin of error, corroborating the acid-base reaction pathway. This conclusion was further validated with the Raman spectra of pure MoS_4^{2-} and WS_4^{2-} species (**Figure S2**).

The chemistry of thiometallate complexes has been investigated extensively, and it is known that tetrahedral MoS_4^{2-} and WS_4^{2-} anions dimerize in solution to form the dinuclear complexes, $Mo_2S_7^{2-}$ and $W_2S_7^{2-}$, which can then undergo a series of rearrangements that involves intramolecular redox reactions (**Scheme 1**).[18–21]
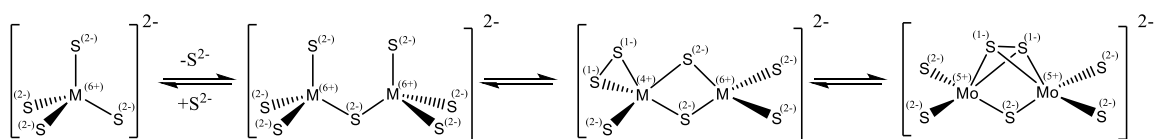

Scheme 1 | Dimerization and internal redox transformations in MS_4^{2-} species (M: Mo, W)

The formation and rearrangement of these dinuclear complexes are accompanied by a ligand-to-metal charge transfer (LMCT), with the reduction of M^{6+} to reduced states and concomitant oxidation of S^{-2} to S^{-1}. This charge transfer is the source of the intense coloration of the dissolved thiomolybdate and thiotungstate complexes, and the accompanying reduction of Mo^{6+}/W^{6+} to lower oxidation states is proven with the XPS data in **Figure 1 b** and **c**.

Polysulfide sequestration by the dinuclear thiometallate

As noted above, MS_4^{2-} and $M_2S_7^{2-}$ (M: Mo, W) are the dominant thiometallate species at equilibrium in the electrolyte, which can provide the first line of protection for the freshly electrodeposited Li metal as discussed at depth later. Additionally, the second front of protection is offered by these species as the cell is being charged and most of the

Li$_2$S is oxidized into elemental S. The long-chain polysulfides, S$_x^{2-}$ (x : 4 - 8), are formed as intermediates before the complete oxidation to S$_8$. These species have moderate solubility in the polar ether-based electrolyte and contain neutral S atoms that can react with metallic Li and result in a loss of active Li content. It is established that the M$_2$S$_7^{2-}$ complex can act as an S^0 acceptor.[20,21] Traditionally, the addition of S^0 to M$_2$S$_7^{2-}$ has been achieved from organo di- and trisulfido compounds, respectively, RSSR and RSSSR.[22] The progressive incorporation of S into the Mo$_2$S$_7^{2-}$ dianion leads to a formation of Mo$_2$S$_x^{2-}$ complexes ($8 \leq x \leq 12$), in which the sulfide ligands are eventually oxidized to disulfido groups while the M^{6+} is reduced to 5+ state, as in the [Mo$^{(5+)}_2$(S$_2$)$^{(2-)}_6$]$^{2-}$ extreme case (**Scheme2**).[23,24]
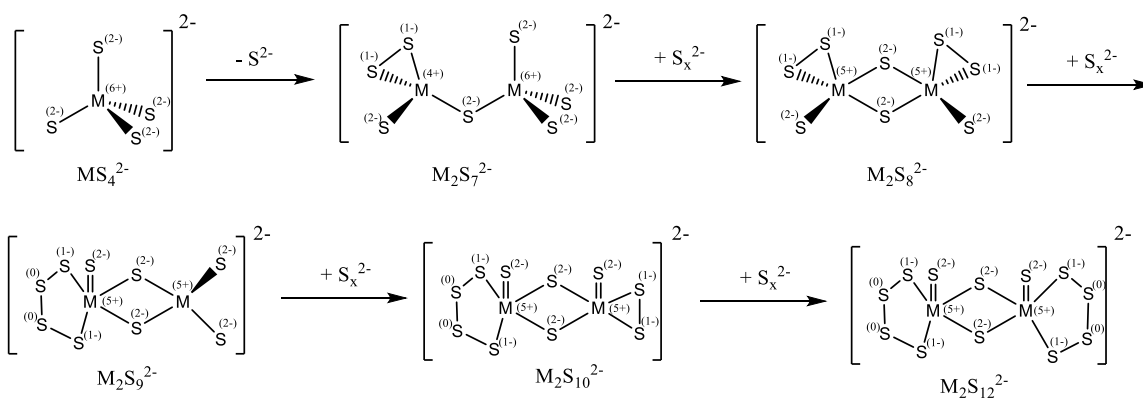


Scheme 2 | Dimerization and subsequent step-wise S^0-atom uptake from oxidized sulfur species by the MS$_4^{2-}$ species.

As the long-chain S$_x^{2-}$ species is potentially the source of S^0, the above reaction implies that each mole of Mo$_2$S$_7^{2-}$ can incorporate up to 5 moles of S^0, leading to the shortening of the length of the S$_x^{2-}$ species by a decreasing (i.e., reducing) the average oxidation state of S atoms. This reduction in chain length is accompanied by their precipitation out of the electrolyte and lowering the likelihood of the hostile encounter

with the Li dendrites. It is worth noting that in the formation of dinuclear $[M_2(S_2)_6]^{2-}$ species, W mimics Mo, as reported previously.[25]

In order to demonstrate the spontaneous S^0 uptake by the tetrahedral MS_4^{2-} species, *in-situ* chronoamperometric analyses were conducted as a solution of Li_2S_8 is brought in contact with $(NH_4)_2MS_4$ (M: Mo, W) salt (**Figure 2a**).
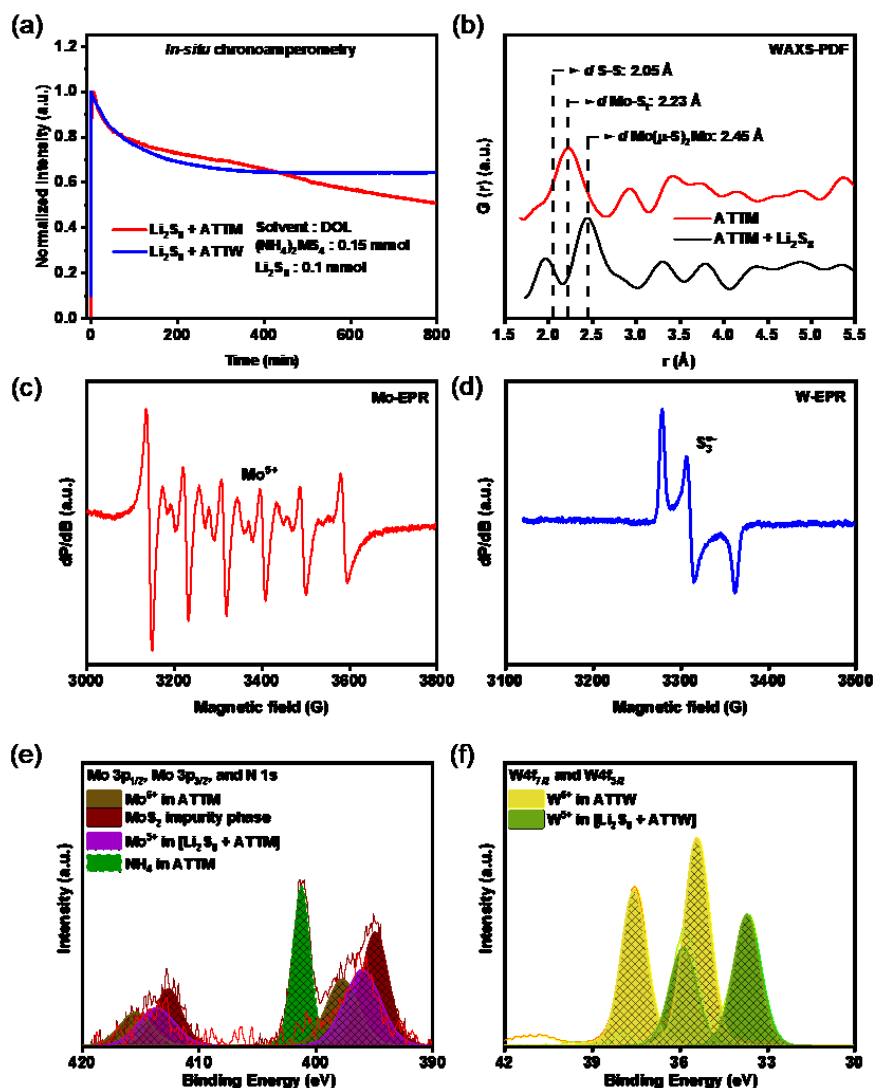
Fig. 2 | Characterization of $(NH_4)_2MS_4 – Li_2S_x$ reaction product in ether-based solvents. a, *In-situ* chronoamperometric analysis of $(NH_4)_2MS_4$—Li_2S_8 reaction rate. **b**, WAXS-PDF analysis of $(NH_4)_2MoS_4$—Li_2S_8 reaction product. **c**, X-band EPR spectrum of the solution-phase reaction product of $(NH_4)_2MoS_4$—Li_2S_8. **d**, X-band EPR spectrum of the solution-phase reaction product of $(NH_4)_2WS_4$—Li_2S_8. **e**, **f**, XPS spectra of $(NH_4)_2MS_4 – Li_2S_x$ reaction product in ether-based solvents (M: Mo, W).

Initially and unlike the case of Li_2S-DOL mixture, the chronoamperometric tests exhibit a non-zero current for the Li_2S_8-DOL solution due to the intermediate oxidation state of S in the S_8^{2-} anion and the facile redox reactions of these species. **Figure 2a** shows the current evolution following the addition of $(NH_4)_2MoS_4$ salt. The monotonic current decay observed in this case implies a reduction in the concentration of S_8^{2-} species through the mechanism outlined above. **Figure 2a** also shows a similar trend for the reaction of S_8^{2-} with $(NH_4)_2WS_4$. Comparing the two additives, it is possible to conclude that the rate of S^0 uptake from S_8^{2-} is faster for the W-containing complex than the Mo counterpart, so that the current reaches a plateau at $\sim$ 70% of I_{max} after 300 minutes. For MoS_4^{2-} additive, despite the slower reaction kinetics, one can attest to a more efficient polysulfide uptake as the current arising from the polysulfide electrochemical interconversion decreases monotonically even after 800 minutes. Based on the above observations, it is evident that the Gibbs free energy change for the formation of a higher S/Mo ratio in the dinuclear Mo-based complex is more negative, while the activation energy for this reaction is higher compared to the $W_2S_7^{2-}$ analog, and therefore the kinetics are slower. Additionally, the ability of thiometallates to sequester S^0 from polysulfides of different orders (Li_2S_n; n = 4, 6, and 8) was tested through chronoamperometric tests. The data in **Figure S3** show that the rate of S^0 uptake by $(NH_4)_2MoS_4$ follows the order $S_8^{2-} > S_6^{2-} > S_4^{2-}$. This highlights that the thiometallates offer an effective defense against higher-order polysulfides, which is essential for Li-S batteries.

To confirm the proposed mechanism of MS_4^{2-} dimerization into $M_2S_7^{2-}$ and the subsequent S^0-atom uptake discussed above, the solid residue from the reaction mixture of

$(NH_4)_2MoS_4/Li_2S_8$ was collected and analyzed through wide-angle X-ray scattering and pair distribution function (WAXS-PDF) analysis. A pure sample of $(NH_4)_2MoS_4$ was also run as a control sample, as shown in **Figure 2b**. The peak at 2.23 Å represents the terminal Mo—S distance in the pristine $(NH_4)_2MoS_4$ crystal (expected 2.18 Å). Comparing the PDF plot of pristine $(NH_4)_2MoS_4$ with the one reacted with Li_2S_8 exhibit sharp contrasts: (i) a new peak at about 2.0 Å emerges indicating the S-S bond in the polysulfide and the disulfido ligands of the dinuclear complex with the peak originally corresponding to Mo-$S_{terminal}$ distance

(2.23 Å) in the pristine ATTM shrinking, and (ii) a new peak emerges at 2.45 Å, corresponding to the bridging Mo—S—Mo in the dinuclear $[Mo_2S_x]^{2-}$ complex (expected 2.40 Å). The above observations indicate the dimerization of the mononuclear MoS_4^{2-} tetrahedral units and the conversion of terminal thio-ligands into bridging analogs.[23]

As a second probe into the reaction mechanism, electron paramagnetic resonance (EPR) spectra were recorded (**Figure 2 c**, **d**). Initially, Mo ions in MoS_4^{2-} are in the diamagnetic 6+ oxidation state and hence are EPR silent (**Figure S4**). On the other hand, the EPR spectrum of MoS_4^{2-} with S_8^{2-} (**Figure 2c**) clearly indicates the presence of paramagnetic species due to reduced Mo species as a result of S^0-atom uptake from S_x^{2-}, according to the sequence of reactions outlined in Scheme 2. The EPR spectrum of MoS_4^{2-}—S_8^{2-} reaction product exhibits at least three paramagnetic Mo species with slight chemical shifts and with a more or less isotropic environment as a result of the varying chemical environment induced by different S/Mo ratios in the gradually growing $[Mo_2S_x]^{2-}$ dinuclear complex. In each case, a sextet EPR signal is observed as a result of the hyperfine splitting of the electron spin transitions by the ^{95}Mo and ^{97}Mo natural isotopes with a nuclear

magnetic moment I = 5/2.[26] **Figure 2d** Also shows the EPR spectrum of the reaction product of $[WS_4]^{2-}$ with S_8^{2-}; similar to the Mo additive, a paramagnetic signal is evident. However, the spin transition signal seems to be originating from an unpaired electron in an anisotropic chemical environment with different principal axes g-values and a nucleus with no magnetic moment (I = 0) due to the absence of the hyperfine interactions. The above evidence points to the presence of $S_3^{\cdot-}$ rather than reduced W species, as also reported previously,[27] in sharp contrast with the Mo counterparts. The absence of paramagnetic W components in the EPR spectrum is also contradictory with the XPS analyses of the solution products (**Figure 2 e and f**), which clearly advocates for both Mo^{5+} and W^{5+} species as a result of dimerization and sequential S^0-atom uptake reactions. A possible explanation regarding the above observation is that cooling down the reaction mixture to 100 K for the acquisition of the EPR spectra shifts the equilibrium constant of dimerization and S^0-atom uptake for the $[WS_4]^{2-}$ species towards the reactants ($\Delta H > 0$), while at the same time increasing the likelihood of $S_3^{\cdot-}$ formation as a result of polysulfide auto-dissociation.

From a theoretical point of view, the tendency of S^0-atom uptake by $Mo_2S_7^{2-}$ was calculated with different Li_2S_x species as the source of S^0 at the DFT level (**Table S1**). The results suggest that the formation of high S/Mo ratio complexes, $Mo_2S_{10}^{2-}$ and $Mo_2S_{12}^{2-}$, is favored compared to the lower $Mo_2S_8^{2-}$ and $Mo_2S_9^{2-}$ homologs, with $Mo_2S_{11}^{2-}$ giving positive formation energy. These results are in-line with the experimental observations that no structure was obtained for the $Mo_2S_{11}^{2-}$ intermediate.[20]

The reaction mechanism for the role of the $(NH_4)_2MS_4$ additive in Li-S cells is depicted schematically in **Figure 3**. It is expected that the acid-base derived introduction

of $(NH_4)_2MS_4$ into the electrolyte (step 1), the subsequent dimerization (step 2), and spontaneous reaction with the soluble polysulfides generated during cell charging (step 3) effectively lead to a reduction of the long-chain polysulfide concentration into the electrolyte (steps 4-6). This is achieved through the incorporation of the oxidized S^0 atoms into the dinuclear complex with partially reduced S atoms and homogenization of the charge disproportionation on the S atoms within the dinuclear complex. This net reduction of the S oxidation state in the S_x^{2-} species reflects in a gradual shortening of the polysulfide chain and their precipitation from the electrolyte and hence minimizing the unwanted reactions at the Li anode.
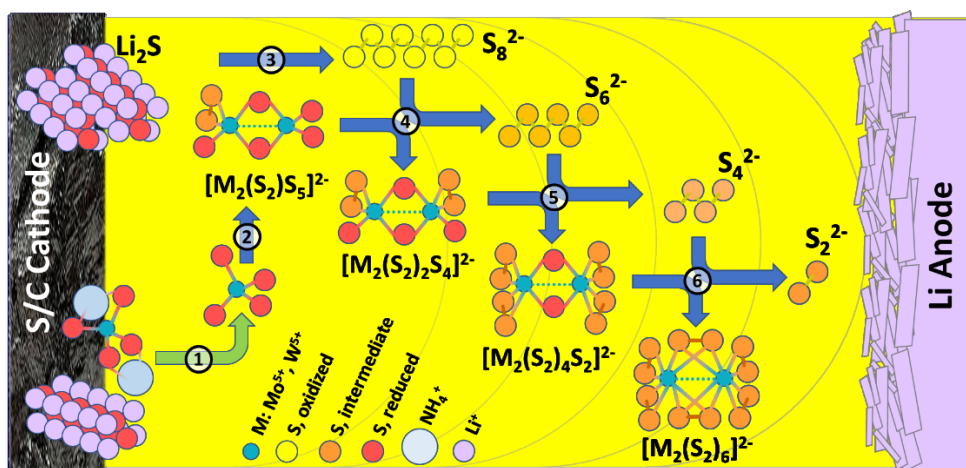
Fig. 3 | A schematic depiction of the introduction of the MS_4^{2-} species into the electrolyte, its dimerization, and spontaneous reaction with long-chain polysulfides through S^0-atom uptake. The acid-base step is shown with a green bent arrow, while those steps involving (intra)intermolecular redox transformations are shown in blue arrows.

**Impact of thiomolybdates and thiotungstates on electrochemical performance**

It was anticipated that the introduction of soluble thiomolybdate and thiotungstate species into the electrolyte of Li-S batteries could have a beneficial impact on electrochemical performance by restraining the active polysulfide in the electrolyte or forming a favorable SEI layer at the anode. To investigate this effect, anode-free full cells

were assembled with [Li$_2$S + 0.05 ATTM/ATTW] cathodes (with a Li$_2$S loading of 4 to 5 mg cm^{-2}) and a bare nickel foil as the anode current collector. Since the only source of active lithium is the Li$_2$S cathode, there is no excess lithium inventory in the anode-free system and its capacity retention depends closely on lithium cycling efficiency.[628] A wet ball-milling process was used to combine Li$_2$S and ATTM/ATTW (20 : 1 molar ratio) with DOL/DME into a fine slurry, and consequently, soluble MoS$_4^{2-}$ and WS$_4^{2-}$ were generated during the cathode preparation step itself.

Figure 4a shows the capacity of anode-free Ni || [Li$_2$S + 0.05 ATTM/ATTW] full cells as a function of cycle number when cycled at C/5 rate. The cycle life of anode-free full cells is significantly improved with the addition of ATTM or ATTW. The control Ni || Li$_2$S full cell with no additive retained 50% of its peak capacity (700 mAh g^{-1}) for 58 cycles. In contrast, the Ni || [Li$_2$S + 0.05 ATTM] full cell retained 50% of its peak capacity (756 mAh g^{-1}) for 150 cycles. The Ni || [Li$_2$S + 0.05 ATTW] full cell retained 50% of its peak capacity (734 mAh g^{-1}) for 164 cycles. This corresponds to an improvement in the lithium inventory retention rate from 98.81% to 99.53% with the addition of ATTM and 99.58% with the addition of ATTW. A similar improvement is also reflected in Coulombic efficiencies (**Figure S5**), which remain stable over extended cycling with the addition of ATTM and ATTW. Overall, the improvement in electrochemical performance is greater with tungsten than with molybdenum. It is interesting to note that the increase in capacity observed in the cells with the additives in the initial cycles could be due to the need for sufficient polysulfide formation and diffusion to occur during cycling to assist in the introduction of thiometallates into the electrolyte. No extraneous voltage plateaus and current peaks are recorded in the charge-discharge profiles (**Figure 4b** and **c**) and cyclic

voltammograms, respectively (**Figure 4d, e and Figure S6**). This also suggests that the addition of ATTM and ATTW to the Li_2S cathode has little impact on cathode redox kinetics. The cycle life was also examined under the C/3 cycling rate (**Figure S7**). Despite the increased current density, similar capacity retention and Coulombic efficiency were observed, thus confirming that the dramatic improvement in the cycle life of anode-free full cells can be attributed to an improvement in lithium cycling efficiency effected by the formation of soluble thiomolybdates ($Mo_xS_y^{2-}$) and thiotungstates ($W_xS_y^{2-}$). To further validate the efficacy of Li protection at scale, anode-free pouch cells were cycled with and without the addition of 0.05 M of ATTW dissolved in the electrolyte (**Figure 4f**). A Li_2S loading of 5 mg cm^{-2} and a lean electrolyte to Li_2S ratio (ELR) of 4 µL mg^{-1} were used to simulate practical high-energy cells. Even with the low dosage of the additives, a 19 % improvement in capacity retention was observed after 50 cycles when compared to the control cell without additives.
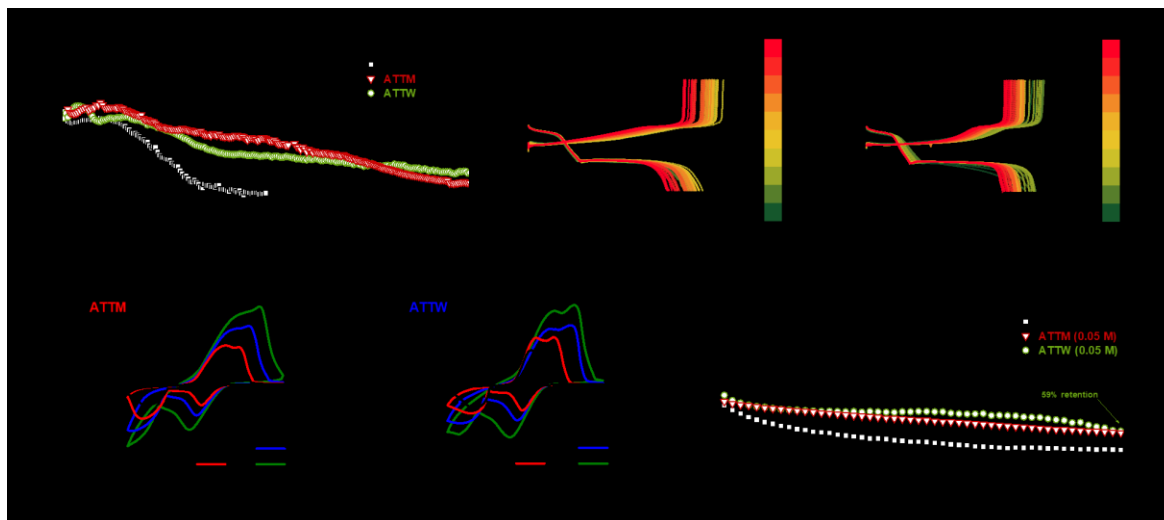
Fig. 4 | Performance of thiometallate additives in anode-free Ni || Li$_2$S cells. a, Long-term cycle life of anode-free cells with different additives. **b, c,** Voltage profiles of cells with, respectively, ATTM and ATTW additives. **d, e,** Cyclic voltammograms of cells with, respectively, ATTM and ATTW additives at different scan rates. **f,** Performance of pouch cells with the additives.

Impact of thiomolybdates and thiotungstates on lithium interfacial chemistry

In order to understand the origins of the favorable impact of thiomolybdate and thiotungstate species on the dynamics of lithium deposition in the Li-S system, the deposited lithium in anode-free Ni || [Li$_2$S + 0.05 ATTM/ATTW] was harvested after 25 cycles and analyzed with time-of-flight secondary ion mass spectrometry (ToF-SIMS). It can be clearly seen in **Figure 5a** that molybdenum and tungsten-containing species are present and uniformly distributed throughout the lithium deposit. These SEI layer components are primarily comprised of Mo and W atoms bonded with sulfur (MoS$^-$/WS$^-$ secondary ions). This is further confirmed with XPS survey scans (**Figure 5b**), which shows an increase in the signal for Mo 3d (~ 240 – 220 eV) and W 4f (~ 40 – 30 eV) peaks with 600 s of sputtering with a monoatomic Ar$^+$ gun, corresponding to a depth of ~ 300 nm. A corresponding increase in the signal for S 2p peaks is not observed, confirming the buildup of Mo/W species with increasing depth in the lithium deposit. Mo 3p region scans with XPS (**Figure 5c**) after sputtering reveal the presence of highly oxidized Mo^{5+} with a binding energy of 397.9 eV, which can be attributed to species with the general formula MoS$_x$O$_y$[29]. Similarly, W 4f region scans with XPS (**Figure 5c**) after sputtering reveal the presence of W^{5+} (in WS$_x$O$_y$) atoms with a binding energy of 35 eV.[30] MoS$_2$ and WS$_2$ are present only as minor components. The presence of some oxygen atoms in the Mo/W-containing SEI layer components (also observed with ToF-SIMS in **Figure 5a**) can be attributed to the highly oxidizing nature of the LiNO$_3$ electrolyte additive, which might donate some of its oxygen atoms to the thiomolybdate/thiotungstate species.[31,32] These partially oxidized thiometallate species, along with inorganic components such as LiF (seen in ToF-SIMS in **Figure 5a)** are the primary components of the SEI. To study the

state of the SEI at different stages of cycling, XPS studies of the Mo 3p and N 1s region were performed on anodes extracted from representative Ni || [Li$_2$S + 0.05 ATTM] cells after the 1st discharge and after 100th charge as shown, respectively, in **Figure S8** and **Figure S9**. At the end of 1st discharge, MoS$_x$O$_y$ and MoS$_2$ species along with LiNO$_3$ and its decomposition products are still observed suggesting that the SEI remains intact and is bound to the Ni foil or the residual, unstripped Li. On prolonged cycling, at the end of 100th charge, the amount of MoS$_x$O$_y$ has reduced while that of MoS$_2$ has increased compared to that at the end of 25th charge. The amount of electrolyte salt decomposition products is also higher. The continued presence of MoS$_x$O$_y$ and MoS$_2$ species suggests that the SEI does remain intact over cycling and are the main contributors towards Li-metal protection. However, the increased decomposition of the electrolyte pointing to the eventual consumption of the additive is the leading cause of lithium inventory loss.

Much like their pure polysulfide counterparts, the thiomolybdate and thiotungstate complexes are generated at the cathode and dissolved in the electrolyte shuttle to the anode, where they are reduced and co-deposited along with metallic lithium during the plating (charging) step. The presence of these thiometallate species as SEI layer components, and the concomitant decrease in the concentration of corrosive polysulfide species in the electrolyte due to their sequestering by dissolved thiometallate complexes, leads to an improvement in the characteristics of lithium deposition. **Figure 5f** shows SEM images of the cycled anodes in anode-free Ni || Li$_2$S full cells. They show a clear improvement in the morphology of the deposited lithium. The mossy high-surface area lithium deposit in the control cell is rendered more homogenous and planar with the introduction of ATTM and ATTW as cathode additives. The mechanism by which the presence of Mo and W atoms

in the SEI layer improves lithium deposition morphology can be understood by the impact they have on lithium diffusion kinetics. Owing to the relatively small difference in electronegativities compared to sulfur (Mo = 2.16, W = 2.38, S = 2.5 on the Pauling scale), these atoms are expected to reduce the electron density around sulfur atoms, facilitating facile lithium migration, especially when compared to Li_2S/Li_2S_2 that are present in the control case. This effect is stronger with W compared to Mo, and as expected, electrochemical performance is better with ATTW as the additive compared to ATTM. The improved lithium deposition morphology leads to fewer side reactions with the electrolyte and mitigates the formation of dead lithium, which translates to reduced lithium inventory loss per cycle, and therefore a three-fold increase in the cycle life of anode-free Ni || Li_2S full cells from 58 to 164 cycles. It is also interesting to note in the ToF-SIMS data that the peak intensity for the different species is reached with less sputtering time for ATTW-based cells compared to the ATTM-based cells suggesting, that the SEI with ATTW is thinner and more compact. This explains the denser Li morphology observed with ATTW compared to the one with ATTM.
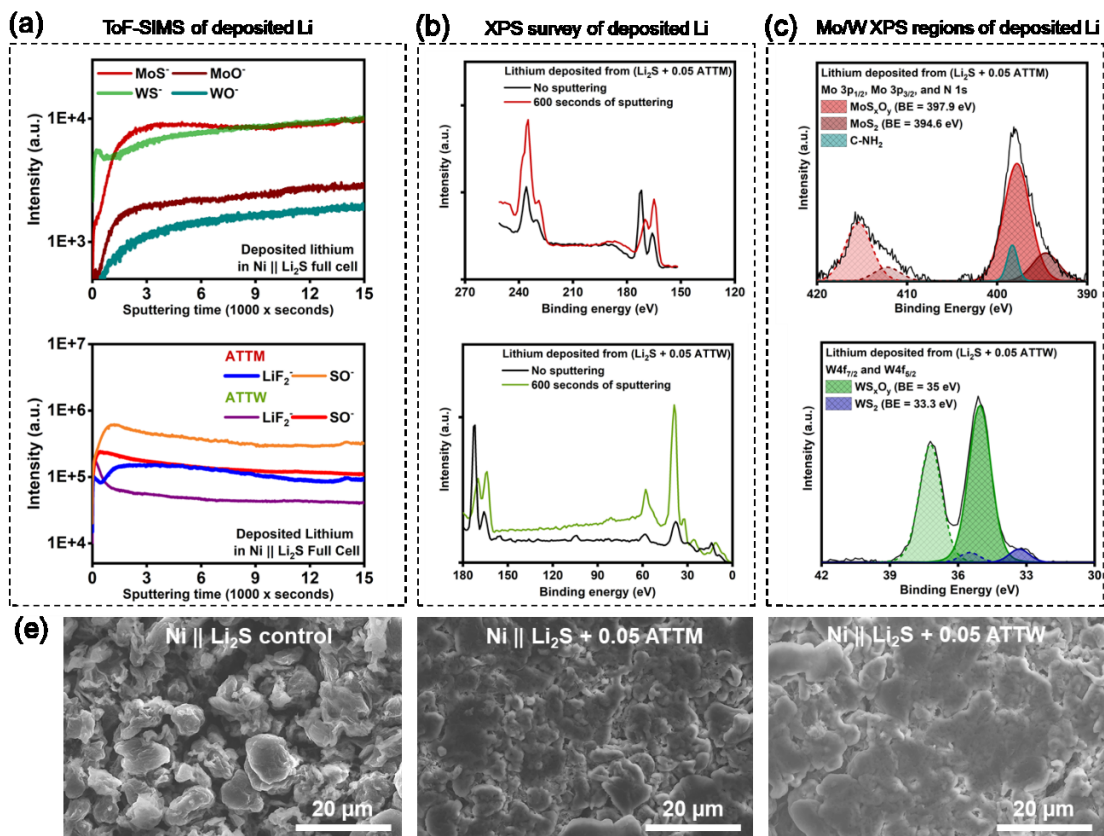
Fig. 5 | Analysis of Li deposited in anode-free Ni || Li₂S full cells. a, ToF-SIMS analysis of different SEI fragments. **b,** XPS survey scans with and without sputtering showing the presence of Mo/W species throughout the SEI. **c,** Mo/W region scans in XPS showing the chemical state of the thiometallate species. **e,** SEM images showing the morphology of the Li deposits on the anodes harvested from anode-free cells after 30 cycles.

Conclusions

This work demonstrates the successful application of ammonium tetrathiomolybdate ((NH_4)$_2$MoS$_4$) and ammonium tetrathiotungstate ((NH_4)$_2$WS$_4$) as cathode additives for improving the cycle life of anode-free Ni || Li₂S full cells. Although not soluble in the ether-based electrolyte in their native state, the tetrathiometallate anions in these additives react with the Li₂S active material and undergo internal rearrangements to form higher-order dimerized thiometallate species that are soluble in the electrolyte. They act as polysulfide buffers, abstracting sulfur atoms from corrosive long-chain

19

polysulfides, converting them into short-chain polysulfides, and reducing their concentration in the electrolyte. At the same time, the crossover of these thiometallate species to the anode leads to their co-deposition with metallic lithium and the formation of a molybdenum and tungsten-enriched SEI layer. These two mechanisms act in tandem to improve lithium cycling efficiency and, therefore, engender a nearly three-fold improvement in the cycle life of anode-free Ni || Li_2S full cells. This work demonstrates a novel pathway towards the realization of practically viable lithium-sulfur batteries with high energy density and long cycle life by employing a limited lithium inventory (N/P ratio = 1). More importantly, in combination with our recent work on selenium and tellurium-substituted polysulfides, this work demonstrates the potency of exploiting the rich chemistry of polysulfides by substituting less electronegative atoms (Mo, W) to improve the performance of lithium-sulfur batteries. The chemistry of thiometallate molecules has been extensively investigated for a wide range of applications, and the approach demonstrated here shows promise of being generalized to substituting other transition-metal and metalloid elements.

Experimental procedures

Resource availability

Lead contact

Further information and requests for resources and reagents should be directed to and will be fulfilled by the lead contact, Arumugam Manthiram (manth@austin.utexas.edu)

Electrochemical measurements

Chronoamperometry tests were performed in glass test tubes fitted with an air-tight septum through which two Inconel wire electrodes are inserted. The test tube was charged with the reaction mixture and constantly stirred during the measurement using a magnet bar (as shown in Figure 1d). A fixed potential of 1 V was applied for all tests using a VoltaLab potentiostat, and the current was measured as the reaction evolved. For the $(NH_4)_2MS_4/Li_2S$ reaction monitoring, 1.4 mmol Li_2S was loaded into the test tube along with 2.0 mL DOL and 0.14 mmol $(NH_4)_2MS_4$ salt, similar in ratio to the starting state of the Li_2S cells. For $(NH_4)_2MS_4/Li_2S_8$ measurements, 0.1 mmol Li_2S_8 was loaded into the test tube along with 2.0 mL DOL, to which 0.15 mmol $(NH_4)_2MS_4$ salts were added. Pure DOL solvent was used in the chronoamperometry tests as no significant difference was found between using pure DOL vs. a DME/DOL mixture. All steps of sample loading and measurements were done in an Ar-filled glove box with O_2/H_2O level below 2.0 ppm. For coin cells, a slurry was made through a rotary milling of Li_2S and multiwall carbon nanotubes (MWCNT) in a ratio of 4 : 1 loaded in a PTFE bottle along with zirconia balls and DME/DOL solvent in a 1 : 1 volume ratio. To this slurry ATTM/ATTW was added such that the Li_2S to ATTM/ATTW ratio was 20 : 1 and milled for 24 h. This slurry was then drop-cast on to an Avcarb P-50 carbon paper with a Li_2S loading of $4 - 5$ mg cm^{-2} and used as the cathode. For pouch cells, the slurry was made by a rotary milling of 70 wt. % Li_2S, 20 wt. % conductive carbon, and 10 wt. %

polyethylene oxide, and polyvinylpyrrolidone-based binder as previously reported. [28,33]

This slurry was blade-casted on to a carbon-coated Al foil (18 μm thick), dried, and then punched into an electrode that is 56 mm (L) x 43 mm (W) with an areal Li_2S loading of 5 mg cm^{-2}. Coin cells were fabricated with cathodes described above, a celgard 2500 separator, and a 30 μm thick Ni-foil as anode. The ELR was maintained at 15 μL mg^{-1}. Single-stack pouch cells were fabricated similar to coin-cells with the cathode described above. An ELR of 4 μL mg^{-1} was used for pouch cells. A uniform stack pressure of 50 psi was applied to the pouch cells during cycling. For the coin cells, the electrolyte used was 1 M of LiTFSI and 0.25 M $LiNO_3$ in DOL/DME (1 : 1 v/v). 0.05 M ATTM/ATTW and 0.1 M Li_2S was stirred in with this electrolyte for 48 h and filtered to yield an additive containing solution that was used as the electrolyte in the pouch cells. All cells were charged first at C/20 to activate the Li_2S before being cycled at the appropriate rate between 2.8 and 1.8 V at room temperature. CVs were collected on a Biologic potentiostat at different scan rates between 2.8 and 1.8 V.

Characterization techniques.

XPS samples were prepared inside a glovebox and transferred in an inert capsule. XPS was performed on a Kratos Axis Ultra DLD spectrometer operating at 12 kV and 10 mA. Pass energies of 20 eV and a 0.1 eV step size was used along with a charge neutralizer and an Ar^+-ion sputtering gun wherever necessary. ToF-SIMS measurements were acquired on a TOF.SIMS 5 spectrometer (ION-TOF) in the negative mode. A 500 eV Cs^+ ion beam was used to sputter the deposited lithium over a sputtering area of 300 x 300 $μm^2$. The analysis was conducted over 100 x 100 $μm^2$. The optical absorption spectroscopy measurements were carried out with a Cary 50 UV-Vis spectrometer in

transmission mode with 10 µm path length quartz cuvettes. The cuvettes were loaded

with the solutions after passing through a 0.2 µm PTFE syringe filter. The cell loading

was carried out in the Ar glove box and carried to the spectrometer in sealed containers

and exposed to air only before the measurement. Similarly, for Raman measurements,

glass capillaries were loaded with test solutions inside the Ar-filled glove box and sealed

on both ends with a polymer clay. Raman spectra were recorded with a Witec Micro-

Raman Alpha 300 spectrometer at 532 nm excitation wavelength. For pair distribution

function analysis, $(NH_4)_2MoS_4/Li_2S_8$ reaction in DOL was allowed to happen for 15 h,

followed by vacuum drying of the reaction mixture. Next, a small portion of the sticky

solid residue, 10 µm in diameter, was dispersed in mineral oil and mounted onto a nylon

loop, which was placed on the goniometer head of an Agilent SuperNova diffractometer

equipped with a monochromatized and micro-focused Mo Kα1 source and an AtlasS2

CCD area detector. The scattering pattern of the sample was collected after dark current

subtraction in the 2θ range of 3.5 – 134° over the course of 13 h, while the sample was

under a continuous purge by a stream of 100 K N_2 gas. The scattering pattern of pristine

$(NH_4)_2MoS_4$ was obtained under identical conditions. The EPR spectra of the

paramagnetic samples were measured at 100 K with a Bruker BioSpin X-band

spectrometer operating at a frequency of 9.4 GHz with a 100 kHz modulated field at an

amplitude of 8.00 G. SEM was performed with a FEI Quanta 650 instrument operated at

10 kV.

Computational methods.

Optimization of the geometry and electronic state of species were carried out at the

density functional theory (DFT) level using the plane-wave basis sets by the quantum

Espresso (QE) code.[34] The nuclear potential of different atomic species was approximated by ultrasoft pseudo-potential (USPP) functionals with electronic exchange-correlation interactions modeled through the generalized gradient approximation (GGA) as parameterized by in the Perdew-Burke-Ernzerhof (PBE) method.[35] A cutoff energy of 544 eV was employed for numerical integration of energy integrals, while the K-space was sampled at the Γ-point. In each case, the molecular anions of $[MS_4]^{2-}$ or $[M_2S_7]^{2-}$ were placed in a dummy cubic cell with an edge of 15 Å and treated as an isolated molecule by applying the Martyna-Tuckerman correction scheme.[36] The solvation of the anionic species was approximated by the implicit continuum solvation model using the Environ module.[37] Respectively, 7.34 and 1.904 were used for static and optical permittivity of DOL, following the reported values.[38,39] Calculation of the absorption spectrum of the neutral Li_2MoS_4 molecule in implicitly modeled DOL was carried out with the time-dependent density functional perturbation theory (TDDFPT) through the Turbo Lanczos module of the QE code.

Data and code availability

All other data and code supporting the findings of this study are available within the article and are described in the Supplemental information or are available from the corresponding author upon reasonable request.

Acknowledgments

Author Contributions

S.N., H.Y and A.B performed the experiments, and A.M. supervised the work. All authors discussed the results and wrote the manuscript.

Declaration of interests

The authors declare no competing interests

References

1. Bhargav, A., He, J., Gupta, A., and Manthiram, A. (2020). Lithium-Sulfur Batteries: Attaining the Critical Metrics. Joule *4*, 285–291.

2. Pang, Q., Liang, X., Kwok, C.Y., and Nazar, L.F. (2016). Advances in Lithium–Sulfur Batteries Based on Multifunctional Cathodes and Electrolytes. Nat. Energy *1*, 16132.

3. Zhao, M., Li, B.Q., Zhang, X.Q., Huang, J.Q., and Zhang, Q. (2020). A Perspective toward Practical Lithium–Sulfur Batteries. ACS Cent. Sci. *6*, 1095–1104.

4.   Hagen, M., Hanselmann, D., Ahlbrecht, K., Maça, R., Gerber, D., and Tübke, J. (2015). Lithium–Sulfur Cells: The Gap between the State-of-the-Art and the Requirements for High Energy Battery Cells. Adv. Energy Mater. *5*, 1401986.

5.   Hou, L.P., Zhang, X.Q., Li, B.Q., and Zhang, Q. (2021). Challenges and promises of lithium metal anode by soluble polysulfides in practical lithium–sulfur batteries. Mater. Today *45*, 62–76.

6.   Nanda, S., and Manthiram, A. (2020). Lithium degradation in lithium-sulfur batteries: Insights into inventory depletion and interphasial evolution with cycling. Energy Environ. Sci. *13*, 2501–2514.

7.   Ng, S.-F., Yu, M., Lau, L., Ong, W.-J., Ng, S.-F., Lau, M.Y.L.W., Ong, -J, Ng, S.-F.W., Sepang, M., Ehsan, D., et al. (2021). Lithium–Sulfur Battery Cathode Design: Tailoring Metal-Based Nanostructures for Robust Polysulfide Adsorption and Catalytic Conversion. Adv. Mater., 2008654.

8.   He, J., and Manthiram, A. (2019). A review on the status and challenges of electrocatalysts in lithium-sulfur batteries. Energy Storage Mater. *20*, 55–70.

9.   Chen, H., Wu, Z., Zheng, M., Liu, T., Yan, C., Lu, J., and Zhang, S. (2021). Catalytic materials for lithium-sulfur batteries: mechanisms, design strategies and future perspective. Mater. Today.

10.   Pluth, M.D., and Tonzetich, Z.J. (2020). Hydrosulfide complexes of the transition elements: diverse roles in bioinorganic, cluster, coordination, and organometallic chemistry. Chem. Soc. Rev. *49*, 4070–4134.

11.   Müller, A., Diemann, E., Jostes, R., and Bögge, H. (1981). Transition Metal Thiometalates: Properties and Significance in Complex and Bioinorganic

Chemistry. Angew. Chemie Int. Ed. English *20*, 934–955.

12. Bag, S., Gaudette, A.F., Bussell, M.E., and Kanatzidis, M.G. (2009). Spongy chalcogels of non-platinum metals act as effective hydrodesulfurization catalysts. Nat. Chem. 2009 13 *1*, 217–224.

13. Tanimu, A., and Alhooshani, K. (2019). Advanced Hydrodesulfurization Catalysts: A Review of Design and Synthesis. Energy and Fuels *33*, 2810–2838.

14. Kibsgaard, J., Jaramillo, T.F., and Besenbacher, F. (2014). Building an appropriate active-site motif into a hydrogen-evolution catalyst with thiomolybdate [Mo3S13]2− clusters. Nat. Chem. 2014 63 *6*, 248–253.

15. Sygellou, L. (2019). An in-situ photoelectron spectroscopy study of the thermal processing of ammonium tetrathiomolybdate, (NH 4) 2 MoS 4, precursor. Appl. Surf. Sci. *476*, 1079–1085.

16. Sun, M., Bürgi, T., Cattaneo, R., Van Langeveld, D., and Prins, R. (2001). TPS, XPS, QEXAFS, and XANES Investigation of the Sulfidation of NiW/Al2O3–F Catalysts. J. Catal. *201*, 258–269.

17. Callahan, K.P., and Piliero, P.A. (1980). Complexes of d8 Metals with Tetrathiomolybdate and Tetrathiotungstate Ions. Synthesis, Spectroscopy, And Electrochemistry. Inorg. Chem. *19*, 2619–2626.

18. McDonald, J.W., Friesen, G.D., Rosenhein, L.D., and Newton, W.E. (1983). Syntheses and characterization of ammonium and tetraalkylammonium thiomolybdates and thiotungstates. Inorganica Chim. Acta *72*, 205–210.

19. Hadjikyriacou, A.I., and Coucouvanis, D. (1987). New Members of the [Mo2(S)n(S2)6-n]2-Series. Synthesis, Structural Characterization, and Properties

of the [Mo2S9]2-, [Mo2S7]2-, and [Mo2S6]2-Thio Anions. Inorg. Chem. *26*, 2400–2408.

20. Hadjikyriacou, A.I., Coucouvanis, D., Enemark, J.H., and Backes-Dahmann, G. (1990). Tetraphenylphosphonium Salts of [Mo2(S) N (s2)6-N]2- Thioanions and Derivatives. In, A. P. Ginsberg, ed. (John Wiley & Sons, Ltd), pp. 39–47.

21. M¨ller, A., Krickemeyer, E., Hadjikyriacou, A., and Coucouvanis, D. (1990). Molybdenum-Sulfur Clusters. In Inorganic Syntheses, A. P. Ginsberg, ed., pp. 47–51.

22. Pan, W.H., Harmer, M.A., Halbert, T.R., and Stiefel, E.I. (1984). Induced Internal Redox Processes in Molybdenum-Sulfur Chemistry: Conversion of MoS42− to MO2S82− by Organic Disulfides. J. Am. Chem. Soc. *106*, 459–460.

23. Clegg, W., Christou, G., David Garner, C., and Sheldrick, G.M. (1981). [Mo2S10]2-, a Complex with Terminal Sulfido, Bridging Sulfido, Persulfido, and Tetrasulfido Groups. Inorg. Chem. *20*, 1562–1566.

24. Draganjac, M., Simhon, E., Chan, L.T., Kanatzidis, M., Baenziger, N.C., and Coucouvanis, D. (1982). Synthesis, Interconversions, and Structural Characterization of the [(S4)2MoS]2−, [(S4)2MoO]2−, (Mo2S10)2−, and (Mo2S12)2− Anions. Inorg. Chem. *21*, 3321–3332.

25. Cohen, S.A., and Stiefel, E.I. (1985). Dinuclear Tungsten(V) and Molybdenum(V) Compounds Containing M2S2(m-S)22+ Cores. Synthesis and Reactivity of [N(C2H5)4]2M2Si2 (M = W or Mo) and the Crystal Structure of [N(C2H5)4]2W2S2(m-S)2(S4)2. Inorg. Chem. *24*, 4657–4662.

26. Schäfer, R., Fiedler, J., Moscherosch, M., and Kaim, W. (1993). First

characterization of a tetrathiomolybdate(V) derivative by EPR, UV–VIS and IR spectroelectrochemistry. J. Chem. Soc. Chem. Commun., 896–897.

27. Vijayakumar, M., Govind, N., Walter, E., Burton, S.D., Shukla, A., Devaraj, A., Xiao, J., Liu, J., Wang, C., Karim, A., et al. (2014). Molecular structure and stability of dissolved lithium polysulfide species. Phys. Chem. Chem. Phys. *16*, 10923–10932.

28. Nanda, S., Bhargav, A., and Manthiram, A. (2020). Anode-free, Lean-Electrolyte Lithium-Sulfur Batteries Enabled by Tellurium-Stabilized Lithium Deposition. Joule *4*, 1–15.

29. Manthiram, A., Sarode, P.R., Madhusudan, W.H., Gopalakrishnan, J., and Rao, C.N.R. (2002). X-ray spectroscopic study of chromium, nickel, and molybdenum compounds. J. Phys. Chem. *84*, 2200–2203.

30. Alsabban, M.M., Min, S., Hedhili, M.N., Ming, J., Li, L.-J., and Huang, K.-W. (2016). Editors' Choice—Growth of Layered WS2 Electrocatalysts for Highly Efficient Hydrogen Production Reaction. ECS J. Solid State Sci. Technol. *5*, Q3067.

31. Nanda, S., and Manthiram, A. (2021). Delineating the Lithium–Electrolyte Interfacial Chemistry and the Dynamics of Lithium Deposition in Lithium–Sulfur Batteries. Adv. Energy Mater. *11*, 2003293.

32. Nanda, S., and Manthiram, A. (2020). Lithium degradation in lithium-sulfur batteries: Insights into inventory depletion and interphasial evolution with cycling. Energy Environ. Sci. *13*, 2501–2514.

33. Nanda, S., Bhargav, A., Jiang, Z., Zhao, X., Liu, Y., and Manthiram, A. (2021).

Implications of in situ chalcogen substitutions in polysulfides for rechargeable batteries. Energy Environ. Sci. *14*, 5423–5432.

34. Giannozzi, P., Baroni, S., Bonini, N., Calandra, M., Car, R., Cavazzoni, C., Ceresoli, D., Chiarotti, G.L., Cococcioni, M., Dabo, I., et al. (2009). QUANTUM ESPRESSO: a modular and open-source software project for quantumsimulations of materials. J. Phys. Condens. Matter *21*, 395502.

35. Perdew, J.P., Burke, K., and Ernzerhof, M. (1996). Generalized Gradient Approximation Made Simple. Phys. Rev. Lett. *77*, 3865.

36. Martyna, G.J., and Tuckerman, M.E. (1999). A reciprocal space based method for treating long range interactions in ab initio and force-field-based calculations in clusters. J. Chem. Phys. *110*, 2810.

37. Andreussi, O., Dabo, I., and Marzari, N. (2012). Revised self-consistent continuum solvation in electronic-structure calculations. J. Chem. Phys. *136*, 064102.

38. Roy, M.N., Ekka, D., Banik, I., and Majumdar, A. (2012). Physics and chemistry of lithium halides in 1,3-dioxolane and its binary mixtures with acetonitrile probed by conductometric, volumetric, viscometric, refractometric and acoustic study. Thermochim. Acta *547*, 89–98.

39. Giner, B., Gascón, I., Villares, A., and Lafuente, C. (2006). Volumetric and refractive properties of binary mixtures containing 1,3-dioxolane and isomeric chlorobutanes. J. Therm. Anal. Calorim. 2006 833 *83*, 735–745.